Cell Metabolism, Volume *15*

Supplemental Information

The Sedoheptulose Kinase CARKL Directs Macrophage Polarization through Control of Glucose Metabolism

Arvand Haschemi, Paul Kosma, Lars Gille, Charles R. Evans, Charles F. Burant, Philipp Starkl, Bernhard Knapp, Robert Haas, Johannes A. Schmid, Christoph Jandl, Shahzada Amir, Gert Lubec, Jaehong Park, Harald Esterbauer, Martin Bilban, Leonardo Brizuela, J. Andrew Pospisilik, Leo E. Otterbein, and Oswald Wagner

Figure S1

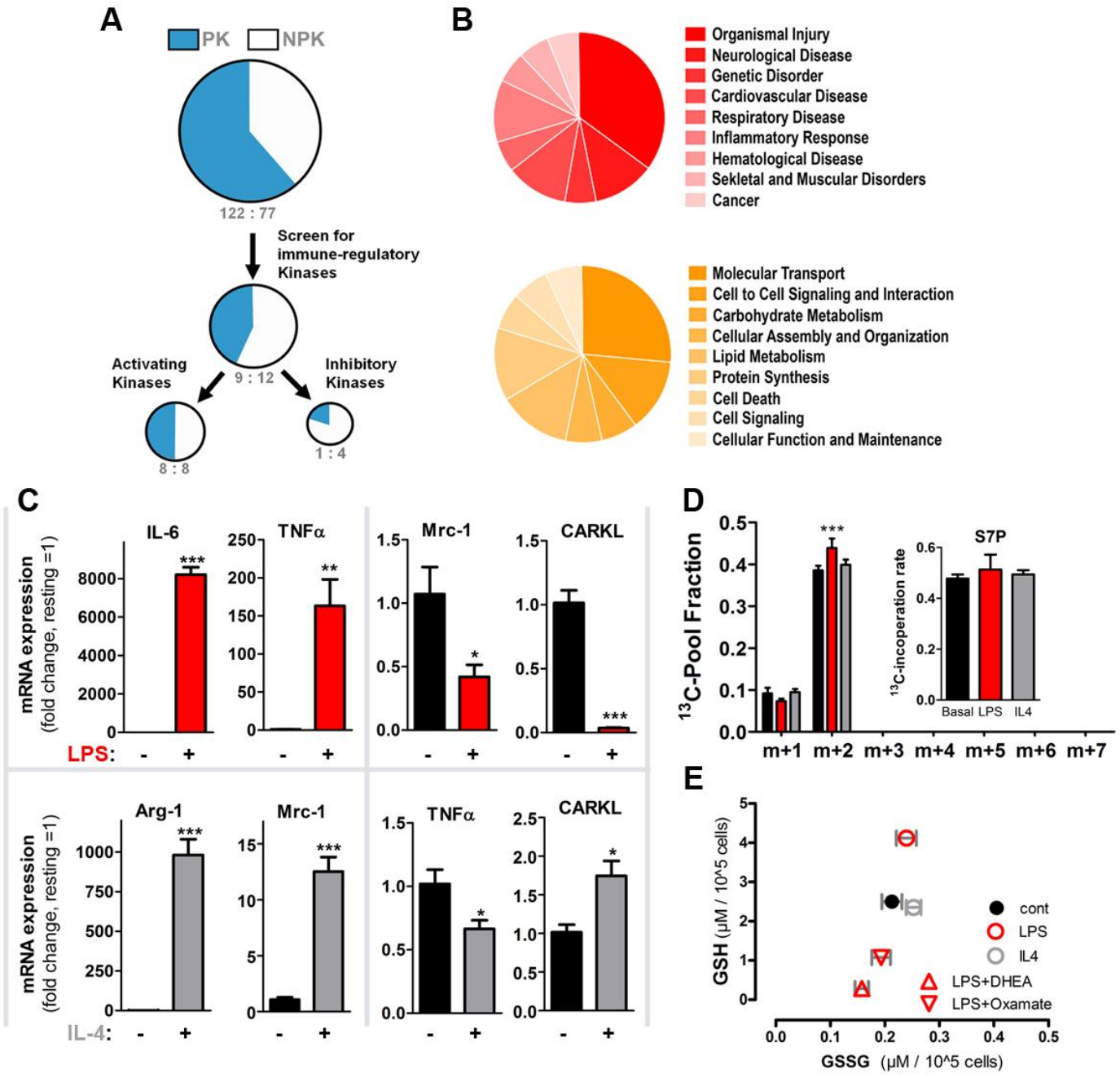
A
PK
NPK
122 : 77
Screen for immune-regulatory Kinases
9 : 12
Activating Kinases
Inhibitory Kinases
8 : 8
1 : 4
B
Organismal Injury
Neurological Disease
Genetic Disorder
Cardiovascular Disease
Respiratory Disease
Inflammatory Response
Hematological Disease
Sekletal and Muscular Disorders
Cancer
Molecular Transport
Cell to Cell Signaling and Interaction
Carbohydrate Metabolism
Cellular Assembly and Organization
Lipid Metabolism
Protein Synthesis
Cell Death
Cell Signaling
Cellular Function and Maintenance
C
mRNA expression (fold change, resting =1)
IL-6
TNFα
Mrc-1
CARKL
LPS: - + - + - + - +
Arg-1
Mrc-1
TNFα
CARKL
IL-4: - + - + - + - +
D
13C-Pool Fraction
m+1 m+2 m+3 m+4 m+5 m+6 m+7
S7P
13C-incoperation rate
Basal LPS IL4
E
GSH (µM / 10^5 cells)
GSSG (µM / 10^5 cells)
cont
LPS
IL4
LPS+DHEA
LPS+Oxamate

Figure S1. Kinase Screen in Macrophages and Activation Induced Metabolism

(**A**) RAW264.7 cells transfected with a human ORF kinase collection were stimulated with LPS. TNFα secretion of stimulated macrophages was analyzed by ELISA. Twenty-one kinases exceeded the screen cut-off of ± 4 standard deviations (~30% change in TNFα production) to determine novel candidate immuno-regulatory kinases. Interestingly, substantial enrichment of non-protein kinases over protein kinases was observed in both the activating and suppressive pools of candidate genes.

(**B**) To gain deeper insight into this observation we performed a gene-ontology based pathway analysis (IPA, Ingenuity Systems) in two contexts. In keeping with the inflammatory nature of the screen the top enrichment scores within the global category *Diseases and Disorders* included "organismal injury and abnormalities", "genetic disorders" and "inflammatory response" (**Table S2**). Analysis under *Cellular and Molecular Function,* interestingly, revealed high scores for genes involved in "molecular transport" and pathways of cell signaling, and notably, carbohydrate and lipid metabolism (lower chart, **Table S3**). Color intensities of pie-charts correspond to enrichment factor which describes the order to robustness of enrichment.

(**C**) We tested primary macrophages for their response to 10 ng/ml IL-4 and 100 ng/ml LPS by monitoring common activation marker and CARKL expression after 4 hrs incubation. Primary BMDMs reduced CARKL upon LPS-activation and simultaneously increased TNFα and IL-6. M2-polarization by IL-4 increased CARKL expression in BMDMs. To ensure an M2-like state we also measured increased arginase 1 (Arg-1) and mannose receptor 1 (Mrc-1) expression, both widely employed activation read-outs for alternatively activated macrophages. M2 marker Mrc-1 is reduced by M1-stimulus LPS, whereas M2-stimulus IL-4 reduces TNFα, a M1-Marker. Data represent mean ± SEM of three independent experiments; *$p < 0.05$, **$p < 0.01$, ***$p < 0.001$.

(**D**) By comparing S7P isotope-distributions a decreased $_{m+1}$S7P and an increased $_{m+2}$S7P fraction were observed. Increased PPP-flux directly forms $_{m+2}$S7P but the origin of $_{m+1}$S7P remains elusive. (insert) S7P showed relatively high incorporation rates (compare to **Figure 1H**) but no significant increase in total flux one hour after LPS activation.

(**E**) PPP activity (by NADPH formation) contributes to reduction of oxidized redox-couples. We expected reduced GSH and NADH regeneration during M1-activation by blocking glucose-flux either by DHEA or by Oxamate. Both GSH and NADH (see **Figure 1H**) were increased during LPS-induced activation (100 ng/ml) accompanied by a moderated increase of the oxidized forms. Glutathione response was measured 4 hrs after stimulation. IL-4 activation operated differently. M2-like activation by IL-4 (10 ng/ml) was not followed by increased GSH formation or NADH formation. During LPS stimulation, CARKL overexpression (**Figure 5D**–**5F**) or direct PPP blocking by DHEA in BMDM, annulled the increase in reduced-factors and resulted in a dramatic redox-shift towards the oxidized state. This clearly indicated the increased turnover of redox-factors during LPS activation in both primary and RAW264.7 macrophages and displayed increased PPP activity as prerequisite to sustain consumption. Thereby we show that redox-regulation is distinctly regulated for either polarization state, correlates with PPP activation and is regulated by CARKL. Data represent mean ± SEM of two independent experiments; *$p < 0.05$, **$p < 0.01$.

Figure S2

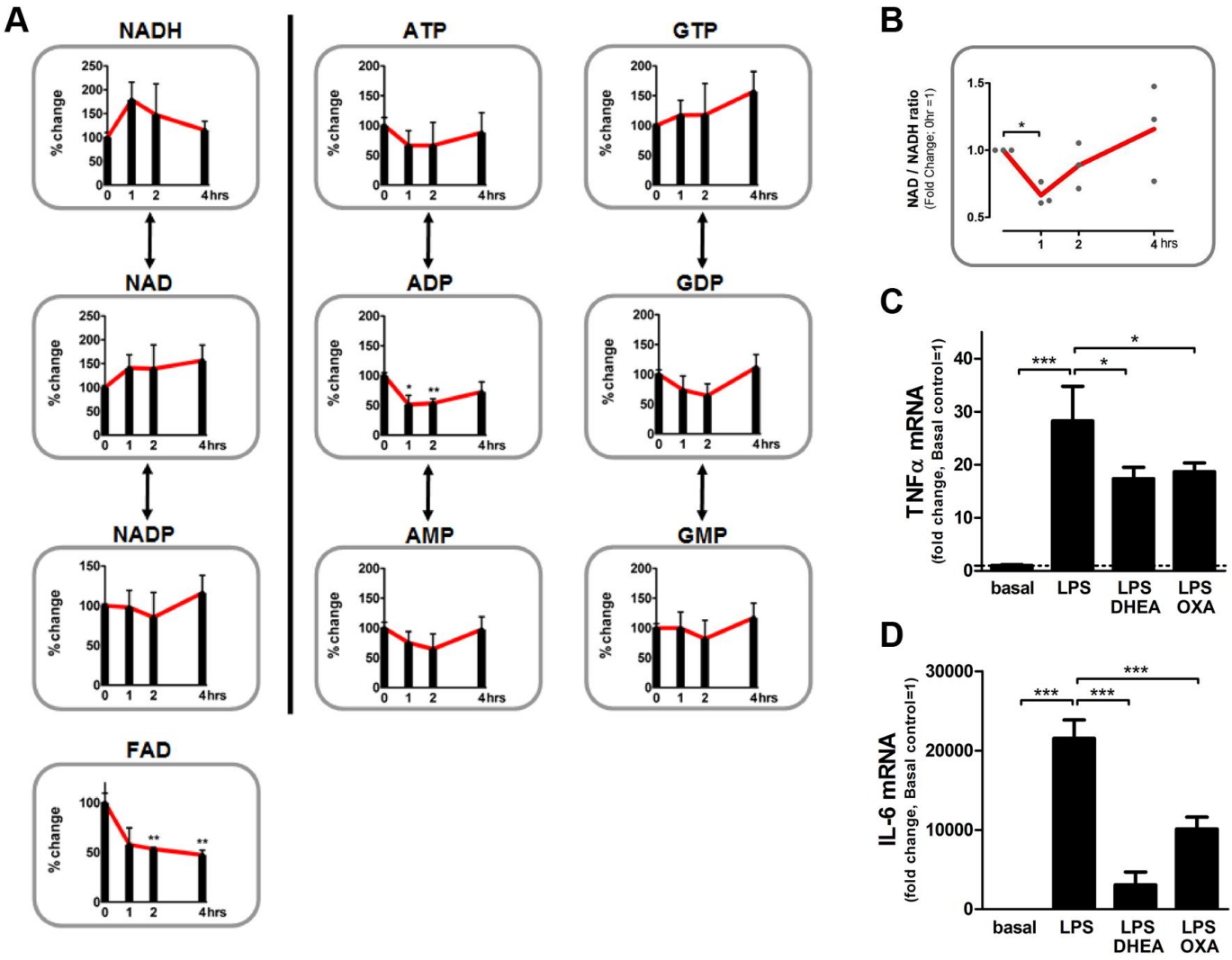
A
NADH
ATP
GTP
NAD
ADP
GDP
NADP
AMP
GMP
FAD
% change
0 1 2 4hrs
B
NAD / NADH ratio
(Fold Change; 0hr =1)
1 2 4 hrs
C
TNFα mRNA
(fold change, Basal control=1)
basal
LPS
LPS DHEA
LPS OXA
D
IL-6 mRNA
(fold change, Basal control=1)
basal
LPS
LPS DHEA
LPS OXA

Figure S2. Metabolic Adaptation during Macrophage Activation

(**A** and **B**) In addition to intermediate metabolites of glucose metabolism depicted in **Figure 2A** we were also able to relatively quantify redox-factors and nucleotides by a metabolomic-time-course during LPS Activation. These additional small molecules are shown in this supplemental figure. pCtrl cells were stimulated with LPS (100 ng/ml) for indicated times. For detailed experimental setup please refer to the main text. (**A**) NAD and NADP levels appeared to be well balanced and not affected by the activation process. FAD levels were significantly reduced. Adenosine (mono-, di-, tri-) phosphates showed substantial decrease although only reduction of ADP was significant. GTP levels trended towards an increase, GDP was similarly regulated as ADP, and GMP remained unchanged. (**B**) NAD/NADH ratios were calculated by peak ratios for each individual experiment over time in fold change (0 hr = 1) and were statistically analyzed by paired t test. The substantial increase in NADH observed in (A) was associated with a rapid drop of the NAD/NADH ratio after macrophage stimulation. The metabolomic data represent the mean peak change in % (untreated cells labelled as 0 hr = 100 %) ± SEM of three independent experiments; to test for significant changes in response to LPS, every time point was analyzed against untreated control (0 hr) by Student's t test; *$p < 0.05$, **$p < 0.01$.

(**C** and **D**) As for RAW264.7 macrophages (**Figure 2D** and **2E**), we tested primary cells for the relevance of this metabolic reconfiguration during M1 polarization in the context of macrophage effector function. We used inhibitors to interfere with glucose-metabolism and measured cytokine production as a functional readout. Both treatments (DHEA and oxamate resulted in a substantial inhibition of M-1 cytokine production as already shown for RAW264.7 cell line. This finding confirmed metabolic-reprogramming (activation of glucose consumption by glycolysis and PPP) as crucial event for proper macrophage M1-polarization. Data represent mean ± SEM of three independent experiments; *$p < 0.05$, **$p < 0.01$.

Figure S3

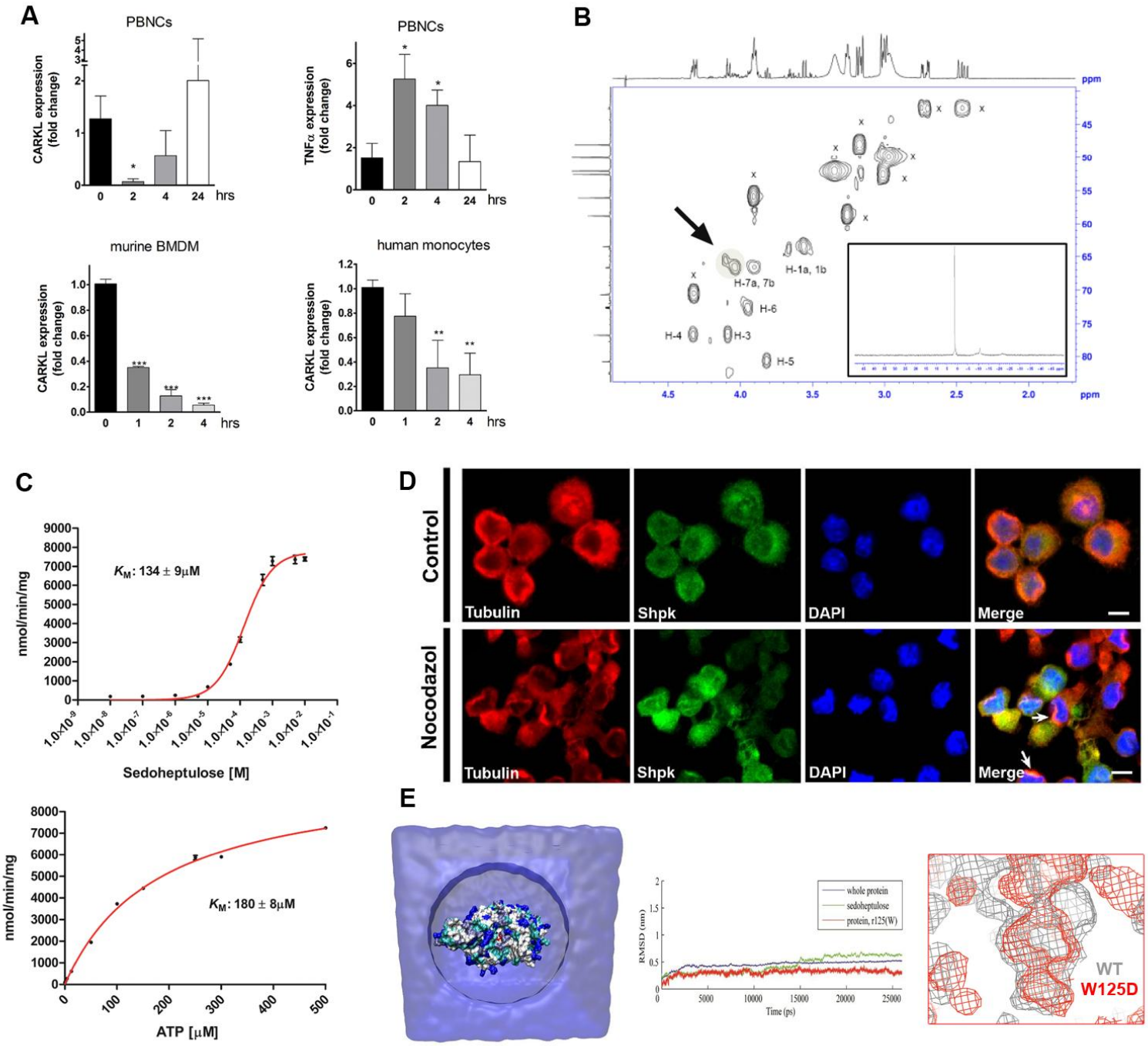
A
PBNCs
CARKL expression (fold change)
hrs
PBNCs
TNFα expression (fold change)
murine BMDM
human monocytes
B
ppm
H-1a, 1b
H-7a, 7b
H-6
H-4
H-3
H-5
C
K_M: 134 ± 9μM
nmol/min/mg
Sedoheptulose [M]
K_M: 180 ± 8μM
ATP [μM]
D
Control
Nocodazol
Tubulin
Shpk
DAPI
Merge
E
RMSD (nm)
Time (ps)
whole protein
sedoheptulose
protein, r125(W)
WT
W125D

Figure S3. CARKL is an Immune-Regulated Sedoheptulose Kinase

(**A**) *In vivo* and *in vitro* CARKL regulation by endotoxin. We injected LPS (50 µg/kg, i.v., n = 3-4) into C57BL/6J mice and examined CARKL and TNFα mRNA expression levels in murine cells. Similarly to the effects of LPS in human PBMCs (**Figure 3A**) we observed a significant CARKL loss in peripheral blood nucleated cells (PBNCs) after *in vivo* stimulation with LPS for two hours (upper left). As a control we also measured TNFα mRNA expression (upper right). In murine bone marrow derived macrophages treated with LPS (100 ng/ml) we observed a very similar and significant down-regulation of CARKL mRNA as seen in the RAW264.7 cell line (**Figure 3B**). To show whether cultured human cells show CARKL regulation comparable to murine cells, we also incubated primary human monocytes with LPS (100 ng/ml) and measured CARKL expression. We observed again a significant loss of CARKL transcript, matching our findings in murine cells. Data represent means ± SEM; *p < 0.05, **p < 0.01, ***p < 0.001**.**

(**B**) $^{1}H/^{13}C$ HSQC spectrum of purified reaction product generated by CARKL (^{31}P-NMR is shown in inset). Assignments are given for the major β-furanose form, signals labeled with x correspond to residual HEPES buffer. Milligram amounts of phosphorylated Sedoheptulose were subjected it to ^{31}P-, ^{1}H-, and ^{13}C-NMR analysis. The assignment of C-7 as the phosphorylation site was deduced from the low-field shifted ^{13}C-signals of C-7 (δ 66.67 and 66.62) and the heteronuclear correlation of the geminal H-7 protons to a single ^{31}P NMR signal at δ 1.34, whereas both geminal protons at C-1 (identified via their HMBC-correlation to the anomeric carbon C-2) were observed at chemical shifts similar to Sedoheptulose. Furthermore, NMR data are in full agreement with recently published data of S-7P generated by a transketolase-catalyzed reaction (Charmantray et al., 2009).

(**C**) We also determined the Michaelis constant K_m for CARKL protein. K_m values were experimentally defined by incubation of recombinant CARKL with various doses of respective substrates. We could ascertain a K_m of 134 ± 9 µM for sedoheptulose (upper graph) and for ATP a K_m of 180 ± 8 µM (lower graph) using an ADP accumulation assay.

(**D**) We evaluated CARKL protein distribution and co-localization in RAW264.7 cells stably expressing CARKL_eGFP in very low quantities. We have shown that CARKL co-localize with G6PD (**Figure 3F**). As many metabolic enzymes, including G6PD,

CARKL co-localized with α-tublin. Cellular distribution of CARKL could be disrupted by nocodazol (20 µM) treatment for 30 min, indicating that CARKL was attached to microtubule filaments. Scale bar equals 5 µm.

(**E**) We generated a structural 3D homology model of CARKL to gain detailed insight into its mechanistic action. Immersed CARKL 3D model in an artificial water bath of 120 Å side lengths (left graphic) used for (middle graph) Molecular Dynamics simulations (real-time of 25 ns). Comparison of the catalytic-cleft of WT CARKL and the W125D mutant form by a mesh-model (right graphic). Mutation of W125 resulted in a deformation of the catalytic-cleft.

Figure S4

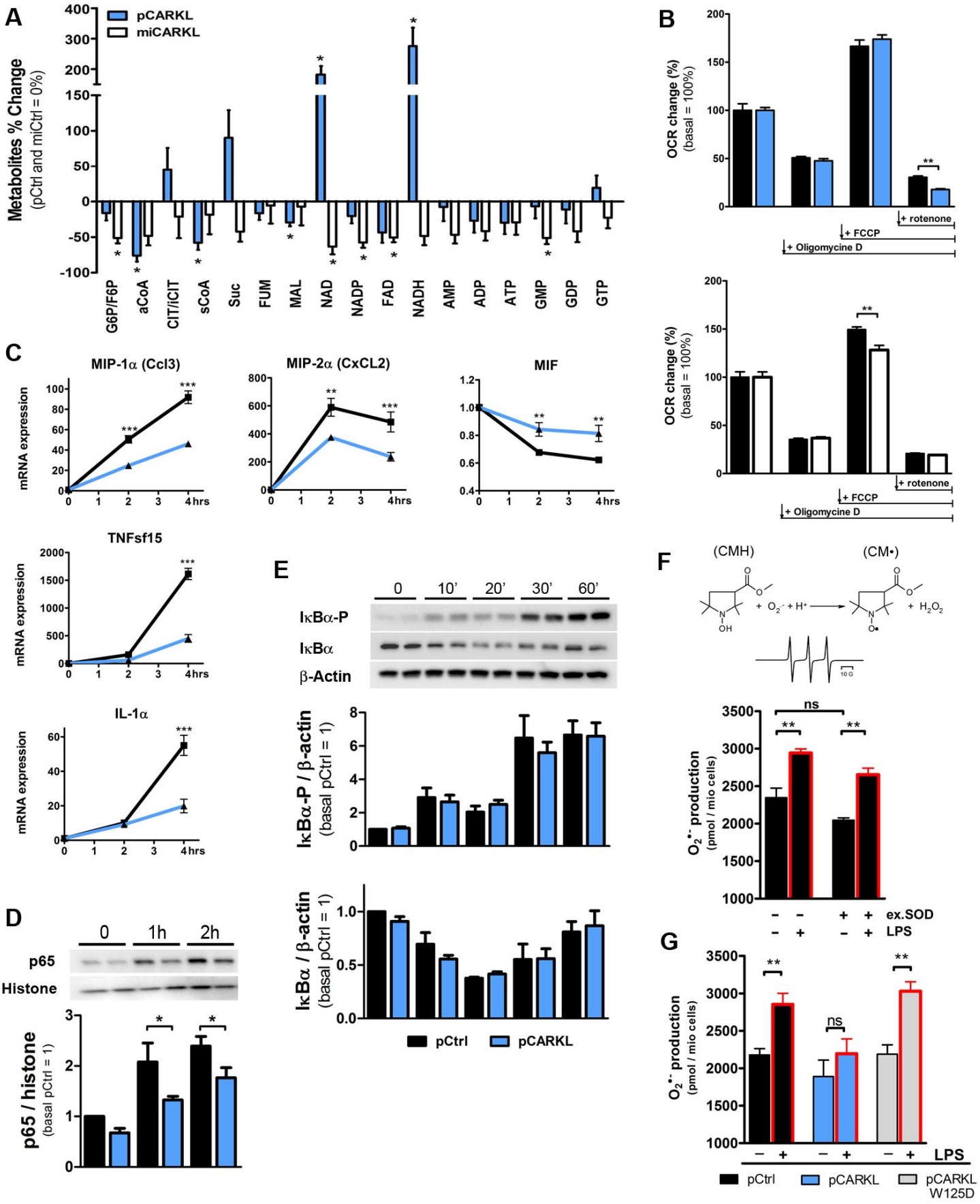
A
pCARKL
miCARKL
Metabolites % Change
(pCtrl and miCtrl = 0%)
G6P/F6P
aCoA
CIT/iCIT
sCoA
Suc
FUM
MAL
NAD
NADP
FAD
NADH
AMP
ADP
ATP
GMP
GDP
GTP
B
OCR change (%)
(basal = 100%)
+ rotenone
+ FCCP
+ Oligomycine D
C
MIP-1α (Ccl3)
MIP-2α (CxCL2)
MIF
TNFsf15
IL-1α
mRNA expression
4hrs
D
0
1h
2h
p65
Histone
p65 / histone
(basal pCtrl = 1)
E
0
10'
20'
30'
60'
IκBα-P
IκBα
β-Actin
IκBα-P / β-actin
(basal pCtrl = 1)
IκBα / β-actin
(basal pCtrl = 1)
pCtrl
pCARKL
F
(CMH)
(CM•)
ns
O2•- production
(pmol / mio cells)
ex.SOD
LPS
G
LPS
pCtrl
pCARKL
pCARKL
W125D

Figure S4. CARKL: Gain and Loss of Function

We compared the relative availability of metabolic intermediates and cofactors in pCARKL and miCARKL cells to their individual control cell lines in %. CARKL perturbations were achieved by stable CARKL overexpression and loss of CARKL by using shRNAmir (**Figure 4A** and **6B**).

(**A**) Using these stable cell lines we assessed changes in the metabolite profile. CARKL overexpression significantly increased the relative concentration of NAD and NADH but reduced acetyl-CoA (aCoA), succinyl-CoA (sCoA) and malate (MAL) levels while AMP/ADP/ATP, GMP/GDP/GTP, fumarate (FUM) and glucose-6-phosphate (G6P) / fructose-6-phosphate (F6P) showed no difference as compared to control cells. In contrast, loss of CARKL protein resulted in a concomitant reduction of G6P/F6P, NAD, NADP, FAD and GMP. These results indicated a strong influence of endogenous CARKL on glucose metabolism by the PPP, glycolysis and the citric acid cycle. Data for sedoheptulose (Sedo), S-7P, G3P, X-5P and R-5P levels are shown in **Figure 4B** and **6C**. Data represent mean % ± SEM of three independent experiments and one sample t-test was used to calculate for significant changes by CARKL perturbation; *$p < 0.05$.

(B) We present Oxygen Consumption Rates (OCR) and Extracellular Acidification Rates (ECAR) as metabolic-measure to assess changes in the cellular bioenergetic-profile (see also **Figure 6D**). By CARKL overexpression Oxygen Consumption Rate (OCR) dropped whereas Extracellular Acidification Rate (ECAR) was not significantly changed. In miCARKL cells we observed also a decrease in OCR but linked with an increase in ECAR, indicating that upon CARKL loss, cells re-route their glucose flux towards glycolysis. To address possible changes in metabolic function (mitochondrial respiration, non-mitochondrial respiration, ATP turnover, H^+ leak and the respiratory capacity) we performed an analysis of OCR after sequential injections of oligomycin (0.8 µg/ml), FCCP (0.4 µM) and rotenone (1 µM) (Nicholls et al., 2010). The pCARKL cell line (upper graph, blue bars) responded to hyperpolarization (oligomycin) and subsequent un-coupling (FCCP) as control cells (black bars). Upon inhibition of mitochondrial respiration (by additional application of rotenone), CARKL overexpression revealed reduced non-mitochondrial (rotenone-resistant) respiration. Plasma membrane based oxygen-consumption is known to account for up to 80% of the entire cellular respiration in certain cell types (Herst and Berridge, 2007). Several

oxidases, including NOX isofroms, were identified as part of a respiratory system located at the plasma-membrane dependent on reducing factors produced by the PPP and glycolysis (Piccoli et al., 2005). This revealed a possible link between CARKL and superoxide ($O_2^{\bullet-}$) formation (see below). An apparent reduction of PPP flux and thereby less potential to reduce oxygen might explain the decrease in non-mitochondrial respiration observed upon CARKL overexpression. In contrast to CARKL overexpression, loss of CARKL caused reduced mitochondrial respiratory capacity suggested by lower FCCP-induced OCR (lower graph, white bars). Further addition of rotenone resulted in the very same rotenone-resistant OCR as observed in control cells (black bars). Thereby, we identified a key difference in regulation of oxygen consumption by either enhanced or reduced CARKL levels. To conclude, reduced CARKL induced ECAR and reduced mitochondrial respiration whereas overexpression blocked non-mitochondrial respiration. Data represent mean % change ± SEM of three independent experiments; *p < 0.05, **p < 0.01.

(**C**) In addition to the LPS-induced gene regulation presented in **Figure 4E**, we further analyzed IL-1α, TNFsf15, MIP-1α, MIP-2α and MIF in pCARKL (blue) and pCtrl. cells as detailed in main text.

(**D** and **E**) In order to verify the regulation of NFκB by CARKL (compare **Figure 4G**), pCtrl and pCARKL cells were stimulated with LPS and Western blot analysis of the p65 subunit of NFκB in nuclear fractions and of IκBα and phosphorylated IκBα (IκBα-P) in complete cell lysates [antibodies were purchased from Cell Signaling #4499 (Histone H3), #8242 (p65), #9246 (IκBα-P) and SantaCruz #sc-847 (IκBα)]. (**D**) p65 band intensities (after 0 h, 1 h, and 2 hrs 100 ng/ml LPS stimulation) were analyzed by densitometric analysis and normalized to the respective Histone H3 band signals (lower panel). The relative nuclear-p65 content in pCtrl (black) and pCARKL cells (blue) as compared to unstimulated pCtrl cells was calculated. Data represent mean fold-change to unstimulated pCtrl cells (± SEM of four experiments; *p < 0.05). (**E**) Total cell lysates of pCtrl (uneven lanes) and pCARKL (even lanes) cells were analyzed in parallel by Western blot for IκBα and IκBα-P protein. Specific bands were analyzed by densitometry and normalized against ß-actin. Fold change to unstimulated pCtrl cells (=1) was calculated [± SEM of two to six experiments per time point; IκBα: upper bar graph; IκBα-P: lower bar graph; pCtrl (black); pCARKL

(blue)]. Interestingly, we observed reduced nuclear p65 in pCARKL cells but no influence on IkBα phosphorylation or degradation.

(**F** and **G**) To test for superoxide ($O_2^{\bullet-}$) production in resting and LPS activated pCARKL cells, we used electron spin resonance (ESR). (**F**) CMH reaction scheme (CMH) 1-Hydroxy-2,2,5,5-tetramethyl-pyrrolidine-3-carboxylic acid methyl ester; (CM•) 3-(Carboxy-methyl)-2,2,5,5-tetramethyl-1-pyrrolidinyloxy. CMH is a highly cell permeable, non-toxic spin probe for the quantification of released intracellular $O_2^{\bullet-}$ production. The resulting nitroxyl radical is resistant to reduction by Vitamin C and thiols. The half-life time of nitroxyl radical in biological environment is about 4 hrs (Fink and Dikalov, 2002). A typical ESR spectrum of oxidized CMH is presented below. To ensure that the increase in $O_2^{\bullet-}$ production during macrophage activation is an intracellular event, we tested the cellular $O_2^{\bullet-}$ response in the presence of extracellular superoxide dismutase (SOD). Increase in $O_2^{\bullet-}$ production by LPS was insensitive to extracellular SOD indicating specificity for the intracellular detection. (**G**) The total $O_2^{\bullet-}$ production of macrophages before and after activation with LPS. Control cells (pCtrl) or cells overexpressing either wild-type CARKL (pCARKL) or the catalytic inactive form W125D (pCARKL W125D) were stimulated for 2 hrs with 100 ng/ml LPS and then analyzed by ESR for $O_2^{\bullet-}$ production. In pCtrl cells we observed increased $O_2^{\bullet-}$ production after LPS activation. This was blocked in pCARKL cells. Overexpression of the catalytic-inactive kinase (CARKL_W125D) showed same increase in $O_2^{\bullet-}$ as control cell line. This finding validated our hypothesis that preserving CARKL-derived-S7P formation during LPS-polarization resulted in a block of intracellular $O_2^{\bullet-}$ formation. This finding directly confirmed the association of CARKL's kinase function (which regulates PPP-flux) with $O_2^{\bullet-}$ production. Data represent means ± SEM of three to four independent experiments; ns = not significant, **$p < 0.01$.

Figure S5

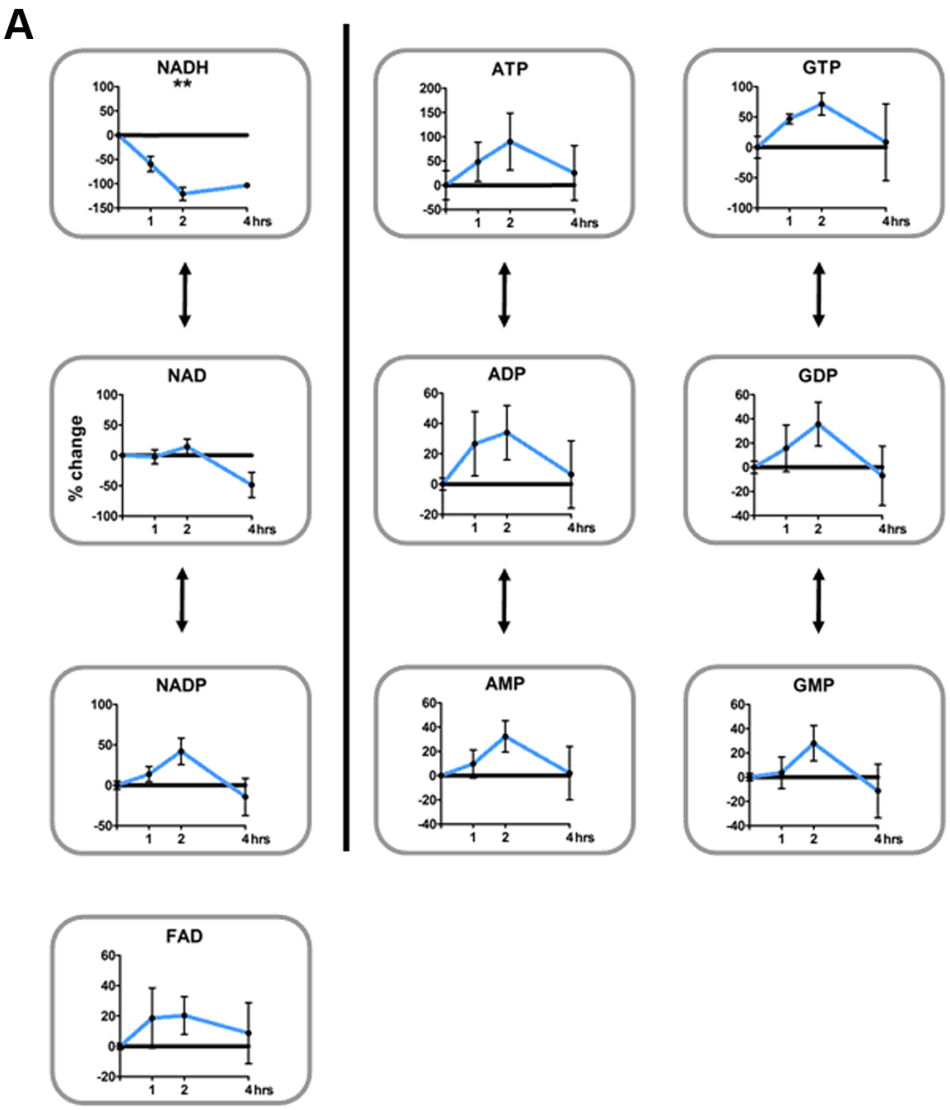
A
NADH
**
ATP
GTP
NAD
% change
ADP
GDP
NADP
AMP
GMP
FAD
1
2
4hrs

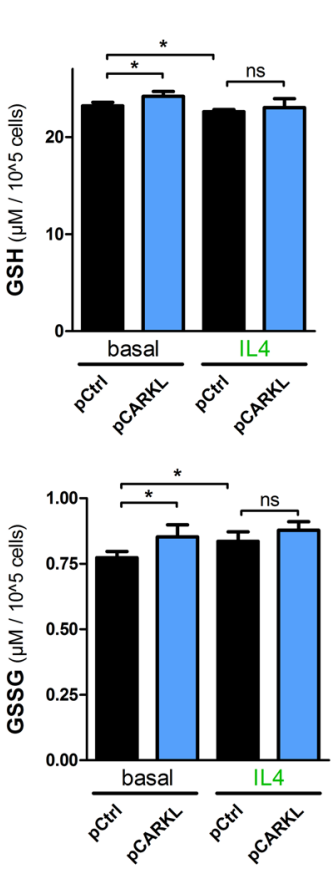
B
GSH (µM / 10^5 cells)
GSSG (µM / 10^5 cells)
*
ns
basal
IL4
pCtrl
pCARKL

Figure S5. Metabolomic-Time-Course and Redox-Adaptation in pCARKL Cells

In addition to intermediate metabolites of glucose metabolism depicted in **Figure 5C,** we were able to relatively quantify certain redox-factors and nucleotides shown in this supplemental figure. To understand which metabolic changes are affected by CARKL loss during macrophage activation we compared the response of pCARKL cells to pCtrl cells after stimulation with LPS (100 ng/ml) for the indicated time spans. The reducing agent NADH was significantly affected by CARKL counter-regulation. Adenosine- and Guanosine triphosphate level showed considerable but not significant changes between pCtrl and pCARKL cells. Data represent delta mean change in % of pCARKL as compared to pCtrl cells (pCtrl = 0%) ± SEM of three independent experiments; to test if a metabolite profile was significantly different between the two groups we used two-way-anova as statistical test (indicated below metabolite name); black line = pCtrl and blue line = pCARKL; **p < 0.01. (**B**) In **Figure 5F** we show LPS-induced macrophage activation to increase cellular GSH significantly. CARKL overexpression during LPS-activation resulted in dramatically increased GSSG (oxidized glutathione) levels compared to the reduced form of glutathione, GSH. Here, we show GSH and GSSG regulation in pCARKL and pCtrl cells before and after IL-4-induced activation (10 ng/ml, 4 hrs). In resting pCARKL cells we observed a small increase in the steady level of GSH (upper graph). Upon IL-4 stimulation, pCtrl and pCARKL cells reduced cellular GSH to comparable levels. The oxidized glutathione was increased in all IL-4 stimulated cells and in resting pCARKL cells if compared to resting control (lower graph). Conclusively these data suggested IL-4 activation to cause consumption of GSH and accumulation of GSSG. CARKL up-regulation resulted in higher basal GSH levels but also in increased GSSG levels. GSSG did not further increase upon IL-4 activation. Of note, IL-4 resulted in up-regulation of CARKL whereas LPS activation in CARKL loss. Data represents means ± SEM; ns = not significant, *p < 0.05, **p < 0.01, ***p < 0.001.

Figure S6

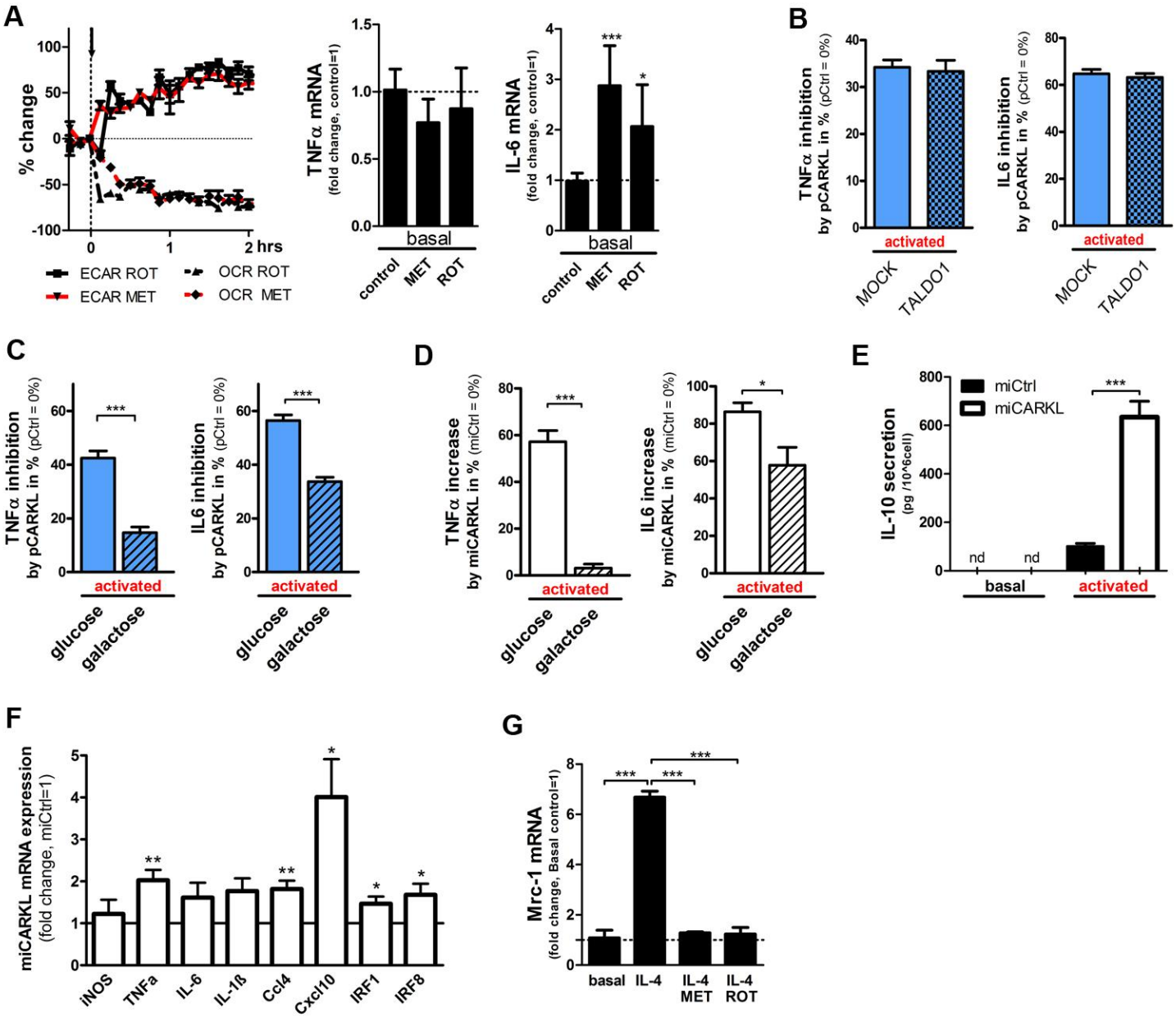
A
% change
2 hrs
ECAR ROT
ECAR MET
OCR ROT
OCR MET
TNFα mRNA (fold change, control=1)
IL-6 mRNA (fold change, control=1)
basal
control
MET
ROT
B
TNFα inhibition by pCARKL in % (pCtrl = 0%)
IL6 inhibition by pCARKL in % (pCtrl = 0%)
activated
MOCK
TALDO1
C
TNFα inhibition by pCARKL in % (pCtrl = 0%)
IL6 inhibition by pCARKL in % (pCtrl = 0%)
activated
glucose
galactose
D
TNFα increase by miCARKL in % (miCtrl = 0%)
IL6 increase by miCARKL in % (miCtrl = 0%)
activated
glucose
galactose
E
IL-10 secretion (pg /10^6cell)
miCtrl
miCARKL
nd
nd
basal
activated
F
miCARKL mRNA expression (fold change, miCtrl=1)
iNOS
TNFa
IL-6
IL-1ß
Ccl4
Cxcl10
IRF1
IRF8
G
Mrc-1 mRNA (fold change, Basal control=1)
basal
IL-4
IL-4 MET
IL-4 ROT

Figure S6. Metabolic Regulation of Macrophage Activation Markers

(**A**) In primary macrophages we further manipulated glucose consumption by incubation with metfromine (15 mM) or rotenone (0.25 µM). Both compounds increased ECAR and decreased OCR. Metformin and rotenone block mitochondrial respiration and thereby enforce non-mitochondrial glucose consumption (line graph). This artificial metabolic-reprogramming was sufficient to induce IL-6 in resting primary macrophages but had no effect on TNF-α expression (bar graphs). In RAW264.7 cells, enforcing metabolic-reprogramming by CARKL knock-down was sufficient to induce TNFα (**Figure 6G** and **6I**).

(**B**) In Figure 6 we showed that LPS-induced cytokine secretion is significantly affected in pCARKL (blocked) and miCARKL (enhanced) cells. For causality testing, we transiently overexpressed transaldolase1 (TALDO1) in pCARKL cells but that did not rescue inhibition of those cytokines.

(**C**) Substitution of glucose (4.5g/L) with galactose (4.5g/L) as the primary carbon source partly rescued TNF-α and IL-6 production in pCARKL cells. This directly implicated metabolic substrate flux as the primary determinant of CARKL's immunomodulatory effects. This was further demonstrated by comparison of cells overexpressing catalytic-inactive or catalytic-active CARKL (**Figure 6A**).

(**D**) Substitution of glucose (4.5g/L) with galactose (4.5g/L) as the primary carbon source reduced enhanced-TNF-α and IL-6 secretion in miCARKL cells.

(**E**) We tested miCARKL cells for IL-10 secretion before and after LPS-activation (100 ng/ml). In the resting state, we did not detect any IL-10. However, LPS-induced IL-10 secretion was enhanced in miCARKL cells 24 hrs after activation. CARKL loss sensitized macrophage M1 polarization not only regarding the pro-inflammatory cytokines TNFα and IL-6, but also affects the late-phase anti-inflammatory cytokine IL-10.

(**F**) Expression profile of commonly used M1 marker genes in resting miCARKL cells compared to miCtrl cells. Importantly, expression all M1 markers with the exception of iNOS, including TNFα, IL-6, IL-1β, Ccl4, Cxcl10, IRF1 and IRF8, were increased in naïve miCARKL cells. This indicated that reduced CARKL expression caused a definitive M1 shift in untreated macrophages. Data represent means ± SEM of at least three independent experiments; ns = not significant, *$p < 0.05$, **$p < 0.01$, ***$p < 0.001$.

(**G**) We tested if pharmacologic activation of glucose consumption, using metformin or rotenone, would alter M2-like polarization by IL-4. Indeed, activation of glucose consumption during IL-4 stimulation resulted in an ablation of mannose receptor 1 (Mrc1) expression, an important marker of M2 polarization. Data in (G) represent mean ± SEM of two independent experiments; *p < 0.05, **p < 0.01, ***p < 0.001. Further, we observed increased Mrc-1 expression in pCARKL cells and reduced levels in miCARKL cells (**Figure 6M** and **6J**). These data based on Mrc-1 expression as readout and metformin or rotenone as tools suggest that elevated glycolysis is disruptive to M2 polarization in primary macrophages.

Figure S7

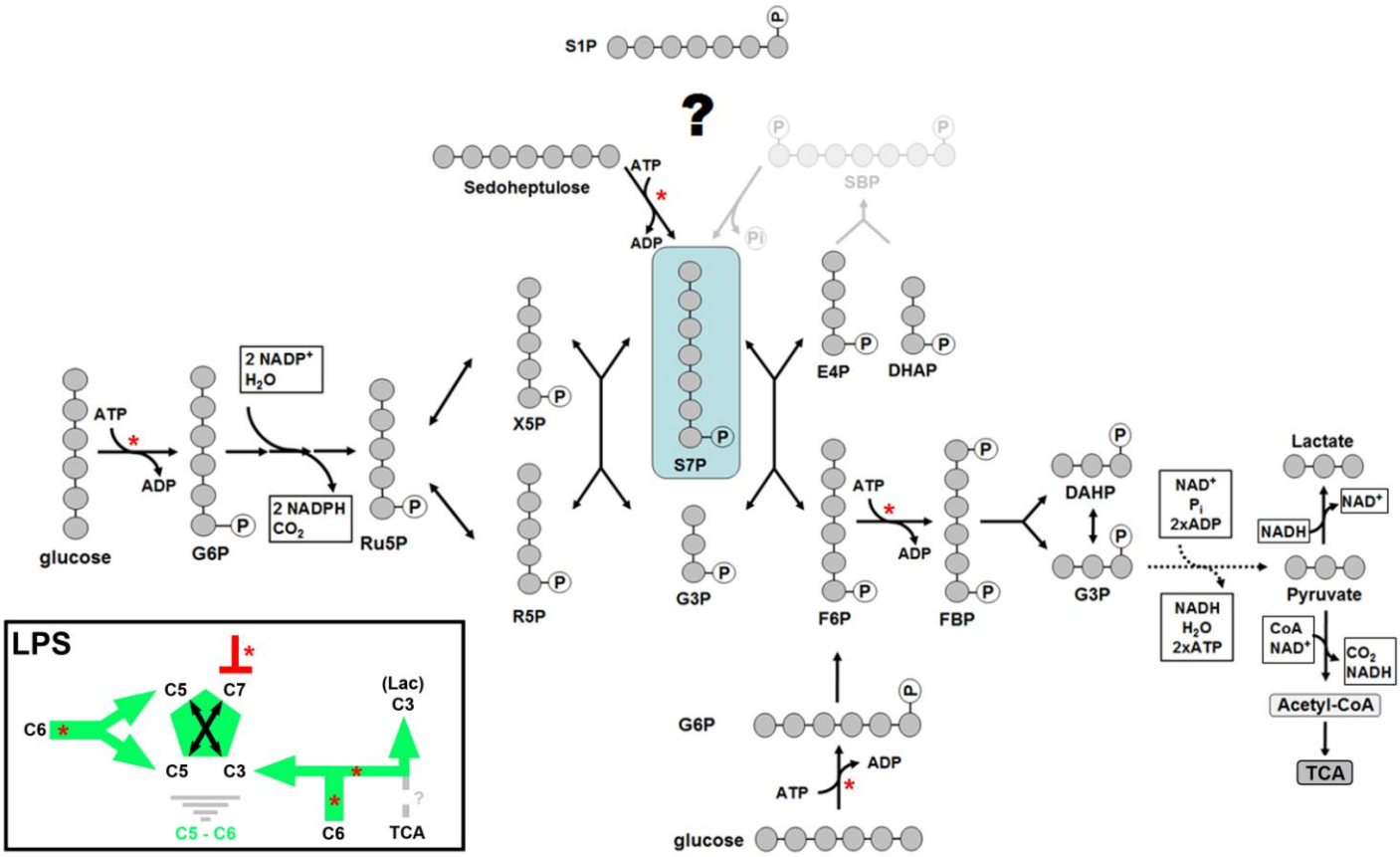
S1P
?
Sedoheptulose
ATP
ADP
SBP
Pi
E4P
DHAP
X5P
S7P
R5P
G3P
F6P
FBP
DAHP
G3P
ATP
ADP
2 NADP+
H2O
2 NADPH
CO2
glucose
G6P
Ru5P
NAD+
Pi
2xADP
NADH
H2O
2xATP
Lactate
NAD+
NADH
Pyruvate
CoA
NAD+
CO2
NADH
Acetyl-CoA
TCA
LPS
C5
C7
C6
C5
C3
(Lac)
C3
C5 - C6
C6
TCA
G6P
ATP
ADP
glucose

Figure S7. CARKL Is a Metabolic Kinase that Integrates Glycolysis and PPP

Simplified schematic illustration of intracellular carbon flux originating from glucose breakdown (indicated by arrows). Inter-conversions of the glycolysis/PPP carbohydrate-phosphate intermediates dihydroxyacetone phosphate (DHAP), G3P, S7P, erythrose-4P, F6P, F-1-6bp and sedoheptulose-1-7-bisphosphate (S1-7bp) are necessary to distribute glucose flux appropriately towards respiration (for energy) and anabolic reactions (nucleotide synthesis and amino acid synthesis) while providing sufficient redox potential to drive numerous cellular processes. Interestingly, in addition to our report on CARKL, a novel sedhoheptulose-1-7-bisphosphatase, which forms S7P from S1-7bp, was very recently reported as a crucial enzyme in yeast ribosome biogenesis with obvious consequences (Clasquin et al., 2011). One outstanding question which remains elusive for the field is how free sedoheptulose is actually formed.

Phosphorylation events (indicated by a red star) in glucose metabolism are rare and primarily used to direct flux orientation by introducing thermodynamically irreversible reactions. In glycolysis this is executed by HK driven phosphorylation of glucose and PFK catalyzed fructose-bisphosphate formation (both enzymes promote glucose consumption and in accordance to our kinase screen enhance also TNFα production). CARKL is the first reported kinase to share a similar role located at the interface of glycolysis and the PPP – the non-oxidative arm of PPP. An important and still partly unresolved issue is the interdependence of CARKL, transketolase and transaldolase in carbon-scrambling events to direct glycolytic and PPP flux.

Knockdown of CARKL increased intracellular G3P, X5P and R5P steady-state levels, in agreement the converse findings in pCARKL overexpressors (**Figure 6C**). In addition, S7P levels were significantly reduced in miCARKL cells whereas the substrate sedoheptulose remained unaffected. Together, these findings fit with the idea that CARKL directly controls flux through the PPP and glycolysis through a simple mass-action process - the constant S7P-feed.

Our data clearly show that even moderate rerouting of glycolytic intermediates towards or away from the PPP is sufficient to skew cell fate of RAW264.7 and primary macrophages. One argument for why enhanced glycolytic/PPP flux could be critical for M1-like polarization is the requirement of NADPH. The oxidative arm of the PPP is a major generator of NADPH, and we demonstrated a dramatic drop in X5P

and R5P metabolite levels following LPS stimulation in RAW264.7 cells (which may reflect enhanced flux through the PPP as seen for flux-analysis in BMDM, see below). Thus, CARKL may block or slow NADPH production through a mass-action process, through the accumulation of S7P. This is supported by the accumulation of X5P and R5P in LPS activated CARKL over-expressing cells (**Figure 5C**). Under these conditions the NAD/NADH ratio increases 10-fold, presumably starving the cell of functionality. The same is true for GSH/GSSG, another redox-couple linked to PPP activity. By CARKL down-regulation we examined a M1-like state in metabolic-parameters (ECAR/OCR, NAD/NADH) as well as in cytokine production. This supports our interpretation of simple mass-action processes regulated by CARKL's S7P contribution to the non-oxidative arm of PPP. During M1 activation loss of CARKL-derived S7P may drive a metabolic-imbalance to enable glycolytic intermediates to fuel PPP. In addition to redox-tuning, this activated PPP generates plenty of C5 and C6 bodies which are also likely demanded for proper M1-activation or for replenishing the carbon-cycle.

Taking a detailed snap-shot of intracellular glucose-flux during LPS-induced activation of bone marrow derived macrophages clearly indicated that M1-like activation increases glycolysis and PPP flux (**Figure 1H** and **1I**). We used dynamic-metabolic-flux measurements taking advantage of asymmetrically labeled ^{13}C-1-2-glucose to allow monitoring not only of pathway flux, but also of origin of the labeled metabolites and thus flux-directionality. To minimize noise from potential carbon-reshuffling under these conditions we used short labeling periods (10min). Using this setup we now directly show that M1-like activated primary macrophages increase glycolytic flux and route a substantial portion into the PPP as indicated by the doubly labeled X5P/R5P (see insert). In our flux analysis we observed high labeling rates for glycolysis/PPP- but very low for TCA-intermediates due to short labeling times. Of note, monitoring IL-4 activation revealed relatively minimal metabolic reprogramming, identifying a key difference between classical and alternative activation modes.

Table S2, Related to Figure 1. Enrichment Analysis: Disease and Disorders

Diseases and Disorders	Enrichment Factor	Robustness Factor	Fisher Exact Test P=
Organismal Injury and Abnormalities	9.48	56.86	< 0.0001
Neurological Disease	3.95	19.74	0.0039
Genetic Disorder	1.94	15.55	0.0381
Cardiovascular Disease	2.79	13.94	0.0215
Respiratory Disease	2.27	13.65	0.0313
Inflammatory Response	3.16	9.48	0.0563
Hematological Disease	1.46	8.75	0.2587
Skeletal and Muscular Disorders	1.69	8.46	0.1862
Cancer	0.82	6.59	0.493
Reproductive System Disease	1.09	6.56	0.7954
Developmental Disorder	1.18	4.74	0.7529
Renal and Urological Disease	1.42	4.26	0.4498
Infection Mechanism	1.24	3.71	0.7165

Table S3, Related to Figure 1. Enrichment Analysis: Molecular and Cellular Function

Molecular and Cellular Function	Enrichment Factor	Robustness Factor	Fisher Exact Test P=
Molecular Transport	6.56	59.04	< 0.0001
Cell-To-Cell Signaling and Interaction	3.69	25.80	0.0008
Carbohydrate Metabolism	2.32	25.48	0.0015
Cellular Assembly and Organization	2.45	19.56	0.0068
Lipid Metabolism	3.16	18.95	0.0054
Protein Synthesis	3.16	15.79	0.012
Cell Death	1.20	15.55	0.3634
Cell Signaling	1.95	13.66	0.0595
Cellular Function and Maintenance	1.68	13.48	0.0958
Cell Morphology	1.90	13.27	0.0647
Post-Translational Modification	1.10	12.07	0.8179
Cellular Development	1.18	10.66	0.6318
Amino Acid Metabolism	0.94	8.43	0.8209
Cellular Movement	1.18	8.29	0.6108
Cellular Growth and Proliferation	0.92	8.25	0.8186
DNA Replication, Recombination, and Repair	1.28	6.40	0.5536
Cell Cycle	1.02	6.09	1

Table S4, Related to Figure 1. Enrichment Analysis: Canonical Pathways

Ingenuity Canonical Pathways	Enrichment Factor	Fisher Exact Test P=
Fructose and Mannose Metabolism	6.77	0.0001
Pentose Phosphate Pathway	5.69	0.0089
Galactose Metabolism	5.41	0.0027
Nitric Oxide Signaling in the Cardiovascular System	4.06	0.0271
Glycolysis/Gluconeogenesis	4.74	0.0049
Fcγ Receptor-mediated Phagocytosis in Macrophages and Monocytes	3.45	0.0188
ERK5 Signaling	3.16	0.0750
mTOR Signaling	3.16	0.0120
Neuregulin Signaling	2.92	0.0351
CNTF Signaling	2.58	0.0961
Growth Hormone Signaling	2.58	0.0961
AMPK Signaling	2.49	0.0348
FLT3 Signaling in Hematopoietic Progenitor Cells	2.03	0.1717
PI3K/AKT Signaling	2.03	0.1717
Aldosterone Signaling in Epithelial Cells	1.67	0.3980
IL-12 Signaling and Production in Macrophages	1.67	0.3980
RAR Activation	1.67	0.3980
Fc Epsilon RI Signaling	1.58	0.4132
NRF2-mediated Oxidative Stress Response	1.58	0.4132
Production of NO and ROS in Macrophages	1.58	0.4132
Thrombin Signaling	1.58	0.4132
Role of Tissue Factor in Cancer	1.50	0.4306
Cardiac Hypertrophy Signaling	1.42	0.4498
Glucocorticoid Receptor Signaling	1.42	0.4498
Role of Macrophages, Fibroblasts and Endothelial Cells in Rheumatoid Arthritis	1.42	0.4498
B Cell Receptor Signaling	1.24	0.7165
Xenobiotic Metabolism Signaling	1.18	0.7241
Role of NFAT in Cardiac Hypertrophy	1.14	0.7327
Molecular Mechanisms of Cancer	0.98	1.0000
Inositol Phosphate Metabolism	0.84	1.0000

Table S5. Primers Used for mRNA Expression Analysis by Q-RT PCR

Gene	Forward Primer (5' to 3')	Reverse Primer (5' to 3')
MOUSE		
ß-Actin	TAGACTTCGAGCAGGAGATGGC	CCACAGGATTCCATACCCAAGA
CARKL	CAGGCCAAGGCTGTGAAT	GCCAGCTGCATCATAGGACT
IL-10	GCCAGAGCCACATGCTCCTA	GTCCAGCTGGTCCTTTGTTTG
IL-6	GGATACCACTCCCAACAGACCT	GCCATTGCACAACTCTTTTCTC
IL-1α	CTCTAGAGCACCATGCTACAGAC	TGGAATCCAGGGGAAACACTG
IL-1β	TGTGCAAGTGTCTGAAGCAGC	TGGAAGCAGCCCTTCATCTT
TNFα	GAACTGGCAGAAGAGGCACT	AGGGTCTGGGCCATAGAACT
TNFsf15	TCCCCGGAAAAGACTGTATG	GCCATCCCTAGGTCATGTTC
MIF	CTGCACCGCTGTTCTTTGAG	ATTTCTCCCGGCTGGAAGGT
IL-13R	ATGGCTTTTGTGCATATCAGATG	CAGGTGTGCTCCATTTCATTCTA
IL-4R	GAGTGAGTGGAGTCCTAGCATC	GCTGAAGTAACAGAACAGGC
iNOS	AATCTTGGAGCGAGTTGTGG	CAGGAAGTAGGTGAGGGCTTG
IRF1	AGGGACATAACTCCAGCACTG	CCTCGTCTGTTGCGGCTTC
IRF8	GGATATGCCGCCTATGACACA	TGCCCCCGTAGTAGAAGCTGAT
TLR4	TCTGGCATCATCTTCATTGTCC	GCGATACAATTCCACCTGCTG
CD11b	CAAGTGCCTGTCACACTGAGC	TGCAACAGAGCAGTTCAGCAC
Cxcl2	AGTGAACTGCGCTGTCAATG	TTCAGGGTCAAGGCAAACTT
Cxcl10	CAGGATGATGGTCAAGCCATG	TTGAGCGAGGACTCAGACCAG
MCP-1 (Ccl2)	AGGTCCCTGTCATGCTTCTG	TCTGGACCCATTCCTTCTTG
MIP-1a (Ccl3)	CACGCCAATTCATCGTTGAC	CATTCAGTTCCAGGTCAGTG
Ccl4	TCCAAGCCAGCTGTGGTATTC	GCTGCTCAGTTCAACTCCAAGTC
MCP-3 (Ccl7)	AGGATCTCTGCCACGCTTC	CCCACACTTGGATGCTGAA
HUMAN		
CARKL	GCCAAAGCTGGAACGTAGAG	CGAGGTGCTGATGTTGAGAA
ß-Actin	CGCGAGAAGATGACCCAGATC	TCACCGGAGTCCATCACGA
TNFα	CAGCCTCTTCTCCTTCCTGA	CAGCTTGAGGGTTTGCTACA

Supplemental Experimental Procedures

Kinase Screen

The human kinase cDNA library was previously generated (Park et al., 2005). Kinase coding sequences in pLP-CMV Neo plasmids for mammalian expression were used for transient transfection of RAW264.7 macrophages. Cells were transfected in 96 well format with 1 µg plasmid in Optimem using Lipofectamine 2000 (Invitrogen) according to the manufacturer's instructions. Each individual kinase was transfected to three wells. Twenty-four hours after transfection, cells were incubated with 100 ng/ml LPS for one hour. Cell-free supernatant was assayed for TNFα production by ELISA . To analyze the effect of each individual kinase we compared the TNFα level of all replicates to control transfection and calculated the change in mean %. For gene-ontology based pathway analysis we used Ingenuity software (IPA Systems). We calculated enrichment factors by dividing the ratios of function/pathway associated kinases of the hit list (n/21 kinases) by associated kinases of the reference list (n/199 kinases). Robustness of enrichment was calculated by multiplication of enrichment factor with the number of kinases (n) from hit list associated with this process. For statistical analysis of enrichments we employed the Fisher Exact Test.

Quantitative RT-PCR

For Q-RT-PCR analysis total RNA was extracted from respective tissues and cells using the RNeasy Mini Kit (Qiagen) according to the manufacturer's instructions. Isolated total RNA was reverse-transcribed into cDNA using commercially available kits (Applied Biosystems). All subsequent Q-RT-PCR reactions were performed on an AbiPRISM 7900HT real-time cycler (Applied Biosystems) using iTaq SYBR Green Supermix with ROX (BioRad). PCR cycling conditions were as follows: initial denaturation at 95°C for 10 min, followed by 40 cycles at 94°C for 15 seconds, 60°C for 15 seconds and 72°C for 1 minute. Post-amplification melting curve analysis was performed to check for unspecific product formation. For normalization, threshold cycles (C_t-values) of all replicate analyses were normalized to β-actin within each sample to obtain sample-specific ΔC_t values. To compare the effect of various treatments with untreated controls, $2^{-\Delta\Delta Ct}$ values were calculated to obtain fold

expression levels. SOCS1 and SOCS3 primer sequences were previously published (Dalpke et al., 2001). All other primers used are listed in **Supplementary Table 5**.

Generation of Recombinant Mutant and Wild-Type CARKL

To generate recombinant CARKL we employed *in vivo* site directed biotinylation as purification strategy. The full length open-reading-frame of mouse CARKL (GenBank™ accession number NP_083307) was cloned into PinPoint Xa-1 vector (Promega) by using 5'NurI and 3'NotI restriction sites. CARKL, including a 3' stop codon, was thereby flanked 5' with a biotin purification tag coding sequence and a Factor Xa protease recognition site. The final construct was verified by sequencing to ensure sequence integrity. The vector was transformed into E. coli BL21(DE3). Protein expression and preparation of bacterial extracts were performed according to PinPoint manual (Promega). Biotin-tagged protein was purified on SoftLink avidin resin (Promega) column by gravity flow. CARKL was eluted with 5 mM Biotin und cleaved by Factor Xa protease to free CARKL entirely from the tag. Factor Xa was removed using a Factor Xa binding resin (Novagen) and recombinant CARKL was ultrafiltrated (cut off 30kDa). To remove endogenous bound Sedoheptulose, recombinant proteins were dialyzed against buffer containing 20 mM HEPES, 250 mM NaCl, 4 mM DTT and 0.005% NP-40. Protein concentration was estimated by measuring absorbance at 280 nm assuming an extinction coefficient of 1.18 $(mg/ml)^{-1}$ cm^{-1} for CARKL.

Sedoheptulose Isolation from *Sedum Spec*.

Sehoheptulose was isolated according to a modified protocol of Schmidt et al (Schmidt et al., 1998). Briefly, Leaves of *Sedum Spec*. were grinded and mixed with an equal volume of water. Crude leave mix was pressed and the liquid passed through a 0.45 µm filter. Pre-cleared extract was incubated for 10 min at 37 °C with activated carbon. After removal of carbon the extract was concentrated by vacuum centrifugation. The concentrate was deproteinized by mixing with 50 °C pre-heated absolute EtOH. The resulting solution was cleared by centrifugation and again concentrated by vacuum centrifugation. For further removal of contaminants the extracts were passed over a Dowex AG1X8 (HCO_3^- form) column and concentrated. The final Sedoheptulose preparation was ~90% pure as measured by NMR analysis (data not shown).

Purification and Characterization of Sedoheptulose-7P

For preparative generation of S7P we incubated 10 mM sedoheptulose with 8 µg/ml recombinant CARKL in a kinase reaction buffer pH 7.6 containing 25 mM HEPES, 20 mM KCl, 10 mM $MgCl_2$ and 10 mM ATP overnight at 30°C. The reaction mixture was applied on a Bio-Gel P2-column (Bio-Rad; 40cm length, 1.6cm in diameter), flushed with water (LiChrosolv Merck) and the flow-through was fractionated in 0.5 ml intervals. Each fraction was tested for the presence of S7P by thin layer chromatography in junction with anisaldehyde/H_2SO_4 stain. S7P containing fractions were pooled and lyophilized for further NMR analysis.

Nuclear Magnetic Resonance (NMR)

NMR spectra were recorded at 297 K on a Bruker DPX 400 instrument at 400.13 MHz for ^{1}H, 100.62 MHz for ^{13}C and 161.97 MHz for ^{31}P using a 5 mm broad band probe with z-gradients. The sample contained freeze dried material dissolved in 600 µl of D_2O in a 5 mm NMR tube. The ppm scales were calibrated to 2,2-dimethyl-2-silapentane-5-sulfonic acid for ^{1}H (0.00 ppm), external 1,4-dioxane for ^{13}C (67.40 ppm) and H_3PO_4 for ^{31}P (0.00 ppm). NMR spectra were recorded using Bruker standard homo-nuclear pulse programs, such as COSY and mlevph. For hetero-nuclear experiments, Bruker standard pulse programs were used, such as HSQC for one bond $^{1}H/^{13}C$ and $^{1}H/^{31}P$ correlations and HMBC for multiple bond proton-carbon correlations. All homo-nuclear and hetero-nuclear spectra were recorded with 1k x 1k data points and zero filled in both dimensions.

3D-Modelling and Docking Experiments of CARKL

The model of CARKL was built based on the 3D structure of Xylulose Kinase (PDB code: 2ITM) by using MODWEB for homology and comparative modeling of protein three-dimensional structures (Eswar et al., 2003; Pieper et al., 2009). The generated model was further optimized and validated by employing a Molecular Dynamics simulation using Gromacs (Lindahl et al., 2001) by applying the following procedure: We immersed the generated model into an artificial water bath of 120 Å side length allowing for a minimum distance of 20 Å (Omasits et al., 2008) between box boundary and Sedoheptulose and applied periodic boundary conditions. Subsequently, we performed an energy minimization of the system using a steepest

decent method as implemented in Gromacs and then increased the system temperature up to 310 °K. Finally, we carried out a Molecular Dynamics simulation for a real-time of 25 ns and performed the RMSD calculations using the built-in analyses tools of Gromacs (**Figure S3E**). For Sedoheptulose positioning within CARKL we employed an automated docking tool AutoDock Vina (Trott and Olson, 2010) to identify receptor – ligand interactions. First, we positioned an optimized Sedoheptulose model into the cavity of CARKL and then defined flexible AA within close proximity to Sedoheptulose (W125, Q126, D257, L258, S279, V280 and L282). AutoDock Vina was adjusted to the following parameters: exhaustiveness = 400, num_modes = 15, energy_range = 60. Flexible docking was calculated for 15 Sedoheptulose/flexible-AS coordinates, which resulted in a binding affinity range of sedoheptulose to the CARKL model between -7.6 to -6.8 kcal/mol. Protein structures were graphically illustrated with PyMOL from Delano Scientific LLC (www.pymol.org) or UCSF Chimera (Pettersen et al., 2004).

Silver Stain

Recombinant CARKL protein was separated on 4-12% polyacrylamide gels (Invitrogen) followed by over night fixation in 50% MeOH / 10% acetic acid. Gel were washed two times for 10min in 50% MeOH and subsequently sensitized with a incubation in 0.02% Sodium thiosulphate for 30 s and two times shortly rinsed with H_2O. Staining was performed in the dark for 20min with a 0.1% silver nitrate solution which was freshly prepared. After a short wash with H_2O gels were developed in a 3% sodium carbonate solution containing 0.05% formaldehyde. Reaction was stopped by incubation with 1% acetic acid.

Cloning and Generation of Stable Cell Lines

To generate a construct for overexpression of CARKL in mammalian cells we cloned a sequence verified murine CARKL cDNA (clone MMM1013 OpenBiosystems) lacking 5’ and 3’ UTRs into pcDNA6 (Invitrogen). Transfection of RAW264.7 cell with empty pcDNA6 or pcDNA6_CARKL was achieved by Superfect reagent (Qiagen). Stable cell integrants were selected over 2 weeks by culture in medium containing 10 µg/ml Blasticidin (Invitrogen). Resulting cells containing either pcDNA or pcDNA_CARKL were termed pCtrl and pCARKL, respectively. Constitutive stable CARKL knockdown in RAW264.7 cells was generated by cell transduction with the

miRNA adapted retroviral vector LMP (Open Biosystems). miRNA-adapted short hairpin RNA specific for mouse CARKL generated in pSM2 vector (Open Biosystems, clone ID:V2MM_41673 F4) was subcloned into the LMP vector with XhoI and EcoRI restriction enzymes. Plasmids were verified by restriction site analysis and sequencing. To produce murine virus particles, 293FT cells (Invitrogen) were transiently co-transfected with a vector containing the viral packaging proteins gag and pol, a vector containing env, and either empty LMP or LMP-miCARKL. Vectors containing gag, env, and pol were kind gifts from Evan Rosen (Beth Israel Deaconess Medical Center, Harvard Medical School, Boston, USA). Lipofectamine 2000 (Invitrogen) was used for transfection. Forty-eight hours after transfection, viral supernatants were collected, supplemented with 8 µg/ml Polybrene (Sigma), and used to infect RAW264.7 cells. Stable integrants were selected with puromycin (5 µg/ml) over a period of 2 weeks. Resulting cell lines were termed miCtrl (Control cell line) and miCARKL (shRNAmir targeting CARKL cell line). Knockdown efficiency was verified by Western blotting. A stable cell line expressing a C-terminal CARKL fusion protein to eGFP was generated by subcloning into a pFUSE vector (invivogen) containing the eGFP coding sequence. This expression plasmid is driven by a hEF1-HTLV promoter which allowed very low expression levels. Transfection and selection of stable integrants was performed as described above with the exception that Blasticidin was replaced by Zeocin (500µg/ml; Invitrogen). To have GFP fluorescence negative cells as internal control for a possible auto-fluorescence in laser scanning fluorescence microscopy, the selection process was stopped before a pure culture was obtained. Expression plasmids PinPoint Xa_CARKL (bacterial expression) and pCARKL (eukaryotic expression), containing the mouse CARKL cDNA were mutated using the QuickChange site directed mutagenesis kit II according to the manufacture instructions (Stratagene). Tryptophan at position 125 (W125) and glutamine at position 126 (Q126), both in the substrate pocket of CARKL, were mutated to an aspartic acid (D125) and to a lysine (K126) to generate the following plasmids: PinPoint Xa_CARKL-W125D, PinPoint Xa_CARKL-Q126K, pCARKL-W125D, pCARKL-Q126K. Furthermore, we generated recombinant CARKL with a mutated ATPase domain by replacing threonines 14 and 15 (T14/T15) to methonine (M14) and lysine (K15) residues resulting in PinPoint Xa_CARKL-T14M/T15K plasmid.

Confocal Laser Scanning Microscopy

Stable CARKL_eGFP macrophages were cultured in tissue culture treated glass slides (BD Falcon). Briefly, for immunofluorescence microscopy, cells were washed twice in PBS and exposed to pre-chilled methanol at -20 °C for 45 seconds. Methanol was removed quickly and the coverslips were washed three times with PBS. Fixed cells were blocked overnight at 4 °C or 2 hrs at RT with blocking solution (2% BSA in PBS). Incubation with rabbit polyclonal anti-G6PD (ab993, AbCam), α-tubulin and ß-Actin (T5168 and A5316 Sigma-Aldrich) was performed at RT for 2 hrs followed by four washing steps with PBS 0.05% Tween. Alexa-594 conjugated goat anti-rabbit or anti-mouse antibody (Molecular Probes) was added for 2 hrs at RT in the dark. Nuclei were visualized with DAPI (Sigma-Aldrich). Slides were mounted with moviol and dried overnight at RT in the dark. Specimens were then examined using a Zeiss LSM5 laser scanning Microscope (Carl Zeiss Optics).

Electron Spin Resonance

We employed a CMH (1-Hydroxy-2,2,5,5-tetramethyl-pyrrolidine-3-carboxylic acid methyl ester) spin probe (Noxygen) to measure intracellular and absolute superoxide generation rates of macrophages after activation (**Figure S4F**). Cells (4x 10^6/ml) were incubated with or without LPS (100 ng/ml) in ESR-Krebs HEPES Buffer (Noxygen). After two hours of incubation DTPA (0.2 mM) and CMH (2 mM) were added to cells. Twenty microliters of the incubated cell suspension were aspirated into a Teflon tube (0.9 mm ID) and transferred to a flexline dielectric resonator ER4118X-MD5 (Bruker). Electron spin resonance measurements were started 2 min after mixing at room temperature using a Bruker EMX spectrometer with the following parameters: microwave frequency 9.685 GHz, modulation frequency 100 kHz, modulation amplitude 1 G, time constant 0.082 sec, center field 3446 G, scan rate 71 G/min, sweep 100 G, sweep time 84 s, receiver gain 2 $\times 10^4$. Always five consecutive scans were recorded and from the increase in the peak-to-peak intensity of the middle line from the resulting nitroxyl radical CM• the CHM oxidation rates were calculated. Absolute CM• concentrations were obtained by comparison with a calibration curve constructed from different CP• (3-carboxy-proxyl) concentrations.

Metabolomic Analysis

Cells were grown in 150 mm dishes and harvested after three PBS washes by centrifugation. The pellet was then frozen in liquid nitrogen and thawed in ice water to support cell lysis. Extraction solvent, which consisted of 100 µl of ice-cold 80/20 methanol/water containing 10 µM $^{13}C_6$-citric acid and $^{13}C_2$-succinic acid as internal standards, was added to the cell pellet, and the pellet was disrupted by probe sonication using a Branson Sonifier 450 (Danbury, CT) set at 20% duty cycle and 40% output power. The sample was sonicated for 20 seconds, followed by a 30 second rest period and then 20 additional seconds of sonication. The sample was then centrifuged at 14000 g at 4°C for 10 min, and the supernatant was transferred to an autosampler vial for analysis by LC-MS.

Samples prepared as described above were separated via hydrophilic interaction liquid chromatography (HILIC) and detected online using tandem mass spectrometry (MS/MS). The HILIC separation was carried out using an Agilent 1200 Rapid Resolution LC system (Agilent, Santa Clara, CA) and a Phenomenex Luna NH_2 (3 µm, 150 mm x 2.1 mm i.d.) column (Phenomenex, Torrance, CA). Mobile phase A was acetonitrile, and mobile phase B was 5 mM ammonium acetate in water, adjusted to pH 9.9 with ammonium hydroxide solution. The gradient was 60%/40% (A/B) to 100% B over 18 min, followed by a 18 sec hold at 100% B. The mobile phase was returned to 60%/40% (A/B) over 0.2 min and was held for 17.5 min for re-equilibration. The flow rate was 0.25 ml/min and the column temperature was held at 25 °C. 8 µl of sample were injected for each analysis.

The LC system was coupled on-line to an Agilent 6410 Triple Quadrupole mass spectrometer with electrospray ionization (ESI) source. The spray voltage was set to -4.0 kV in negative ion mode. The desolvation gas flow rate was 10 L/min, the desolvation gas temperature was 350 °C, and the nebulizer pressure was 40 psi. The LC-MS system was controlled using the Agilent MassHunter Data Acquisition software. Compounds were detected using multiple reactions monitoring (MRM) mode with a 50 ms dwell time per transition. Prior to performing LC-MS analyses, the MS/MS transitions were optimized for detection of metabolite intermediates by flow injection analysis of authentic standard compounds.

Non-Stationary Isotopic Flux Analysis

Cells were grown in 100 mm dishes and at day of experiment stimulated for indicated times. After cell stimulation normal growth media (DMEM high glucose) was removed and replaced with media containing 100% ^{13}C-1-2-glucose instead of unlabeled glucose. Primary macrophages were placed back to incubator for 10 min to reach non-stationary labeling. For quenching, we exactly timed media removal, ddH_2O wash and snap-freezing by pouring liquid nitrogen into the cell plate. Dishes were stored at -80 °C for one week. Carbon-13 mass isotopomer analysis of glycolysis, pentose phosphate pathway, and nucleotide metabolites in cultured cells was carried out using liquid chromatography-mass spectrometry (LC-MS) according to the protocol of (Lorenz et al., 2011). Briefly, metabolites were extracted by adding 1.5 mL of cold 8:1:1 methanol:chloroform:water to the quenched (frozen) cell culture plates and scraping with a cell scraper to release the cells. Cell debris and precipitated proteins were pelleted by centrifugation and the supernatant was directly analyzed by mixed-mode anion exchange – hydrophilic interaction chromatography using a Phenomenex Luna NH2 3µ column, 15 cm x 1 mm ID. Mobile phase A for the separation was acetonitrile and mobile phase B was 5mM ammonium acetate in water (adjusted to pH 9.9 with ammonium hydroxide). The gradient consisted of a 15 min linear ramp from 15% to 100% B, followed by a 2-min hold at 100% B and a subsequent 17-min re-equilibration period at 15% B. The sample injection volume was 20 µL and the flow rate was 0.07 mL/min. Detection was performed by electrospray ionization mass spectrometry in negative ion mode using an Agilent 6220 time-of-flight mass spectrometer. MS parameters were as follows: gas temp 350 °C, drying gas 10 L/min, nebulizer 20 psig, capillary voltage 3500V, scan range 50-1200 m/z. Metabolites were identified in the LC-MS data by comparing accurate mass and retention time of peaks with those of authentic standards. Relative quantitation of each metabolite and all of its isotopes was performed by measurement of peak area from extracted ion chromatograms. Mass isotopomer distributions were calculated by dividing the peak area of each isotope by the sum of the peak area for all detected isotopes.

Supplemental References

Cabezas, H., Raposo, R. R., and Melendez-Hevia, E. (1999). Activity and metabolic roles of the pentose phosphate cycle in several rat tissues. Mol Cell Biochem *201*, 57-63.

Charmantray, F., Hélaine, V., Legeret, B., and Hecquet, L. (2009). Preparative scale enzymatic synthesis of D-sedoheptulose-7-phosphate from ß-hydroxypyruvate and D-ribose-5-phosphate. . J Mol Catalysis B: Enzymatic *57*, 6-9.

Clasquin, M. F., Melamud, E., Singer, A., Gooding, J. R., Xu, X., Dong, A., Cui, H., Campagna, S. R., Savchenko, A., Yakunin, A. F., *et al.* (2011). Riboneogenesis in yeast. Cell *145*, 969-980.

Dalpke, A. H., Opper, S., Zimmermann, S., and Heeg, K. (2001). Suppressors of cytokine signaling (SOCS)-1 and SOCS-3 are induced by CpG-DNA and modulate cytokine responses in APCs. J Immunol *166*, 7082-7089.

Eswar, N., John, B., Mirkovic, N., Fiser, A., Ilyin, V. A., Pieper, U., Stuart, A. C., Marti-Renom, M. A., Madhusudhan, M. S., Yerkovich, B., and Sali, A. (2003). Tools for comparative protein structure modeling and analysis. Nucleic Acids Res *31*, 3375-3380.

Fink, B., and Dikalov, S. (2002). Detection of superoxide with new cyclic hydroxylamine CMH in plasma, cells and isolated heart. Free Radic Biol Med *33*, S366.

Gomez-Sanchez, E. P., Romero, D. G., de Rodriguez, A. F., Warden, M. P., Krozowski, Z., and Gomez-Sanchez, C. E. (2008). Hexose-6-phosphate dehydrogenase and 11beta-hydroxysteroid dehydrogenase-1 tissue distribution in the rat. Endocrinology *149*, 525-533.

Herst, P. M., and Berridge, M. V. (2007). Cell surface oxygen consumption: a major contributor to cellular oxygen consumption in glycolytic cancer cell lines. Biochim Biophys Acta *1767*, 170-177.

Lindahl, E., Hess, B., and Van Der Spoel, D. (2001). GROMACS 3.0: a package for molecular simulation and trajectory analysis. J Mol Model *7*, 306–317.

Lorenz, M. A., Burant, C. F., and Kennedy, R. T. (2011). Reducing time and increasing sensitivity in sample preparation for adherent mammalian cell metabolomics. Anal Chem *83*, 3406-3414.

Nicholls, D. G., Darley-Usmar, V. M., Wu, M., Jensen, P. B., Rogers, G. W., and Ferrick, D. A. (2010). Bioenergetic profile experiment using C2C12 myoblast cells. J Vis Exp.

Omasits, U., Knapp, B., Neumann, M., Steinhauser, O., Stockinger, H., Kobler, R., and Schreiner, W. (2008). Analysis of Key Parameters for Molecular Dynamics of pMHC Molecules. Mol Simulat *34*, 781-793.

Park, J., Hu, Y., Murthy, T. V., Vannberg, F., Shen, B., Rolfs, A., Hutti, J. E., Cantley, L. C., Labaer, J., Harlow, E., and Brizuela, L. (2005). Building a human kinase gene repository: bioinformatics, molecular cloning, and functional validation. Proc Natl Acad Sci U S A *102*, 8114-8119.

Pettersen, E. F., Goddard, T. D., Huang, C. C., Couch, G. S., Greenblatt, D. M., Meng, E. C., and Ferrin, T. E. (2004). UCSF Chimera--a visualization system for exploratory research and analysis. J Comput Chem *25*, 1605-1612.

Piccoli, C., Ria, R., Scrima, R., Cela, O., D'Aprile, A., Boffoli, D., Falzetti, F., Tabilio, A., and Capitanio, N. (2005). Characterization of mitochondrial and extra-mitochondrial oxygen consuming reactions in human hematopoietic stem cells. Novel evidence of the occurrence of NAD(P)H oxidase activity. J Biol Chem *280*, 26467-26476.

Pieper, U., Eswar, N., Webb, B. M., Eramian, D., Kelly, L., Barkan, D. T., Carter, H., Mankoo, P., Karchin, R., Marti-Renom, M. A., *et al.* (2009). MODBASE, a database of annotated comparative protein structure models and associated resources. Nucleic Acids Res *37*, D347-354.

Schmidt, U., Stiller, R., Brade, H., and Thiem, J. (1998). Unusual Phosphorylation of Sedoheptulose by Means of Hexokinase. Synlett, 125-126.
Trott, O., and Olson, A. J. (2010). AutoDock Vina: improving the speed and accuracy of docking with a new scoring function, efficient optimization, and multithreading. J Comput Chem *31*, 455-461.